Editors' Suggestion

All-Optical Magnetothermoelastic Skyrmion Motion

Serban Lepadatu*

Jeremiah Horrocks Institute for Mathematics, Physics and Astronomy, University of Central Lancashire, Preston PR1 2HE, UK

(Received 20 January 2023; revised 1 March 2023; accepted 20 March 2023; published 12 April 2023)

It is predicted that magnetic skyrmions can be controllably moved on surfaces using a focused laser beam. Here an absorbed power of the order 1 mW, focused to a spot size of the order 1 μm, results in a local temperature increase of around 50 K, and a local perpendicular strain of the order 10^{-3} due to the thermoelastic effect. For positive magnetoelastic coupling this generates a strong attractive force on skyrmions due to the magnetoelastic effect. The resultant motion is dependent on forces due to (i) gradients in the local strain-induced magnetic anisotropy, (ii) temperature gradients resulting in magnetic parameter gradients due to their temperature dependences, especially local effective anisotropy gradients, and (iii) Magnus effect acting on objects with nonzero topological number. Using dynamical magnetothermoelastic modeling, it is predicted skyrmions can be moved with significant velocities (up to 80 m/s shown), both for ferromagnetic and antiferromagnetic skyrmions, even in the presence of surface roughness. This mechanism of controllably moving single skyrmions in any direction, as well as addressing multiple skyrmions in a lattice, offers an approach to constructing and studying skyrmionic devices with all-optical control.

DOI: 10.1103/PhysRevApplied.19.044036

I. INTRODUCTION

Magnetic skyrmions are disklike topological objects in magnetization textures [1], which can be stabilized using the Dzyaloshinskii-Moriya interaction (DMI) [2,3] in materials lacking inversion symmetry, either in the bulk [4], but also at room temperature in layers with interfacial DMI [5]. Applications have been proposed for skyrmionic devices, including artificial synapses for neuromorphic computing [6], neural networks [7], skyrmionic interconnects [8], probabilistic computing [9], and magnetic memory [10]. Moving skyrmions is typically achieved using electrical contacts, relying on spin torques due to charge and spin currents, including spin-orbit torques [11–13], as well as bulk and interfacial spin-transfer torques [14,15]. Other methods include use of surface acoustic waves (SAWs) generated using interdigitated transducers [16], magnetic field gradients generated using a magnetic force microscopy (MFM) probe [17], thermal gradients generated using on-chip heaters [18], and even the combination of temperature gradients with an externally generated strain has been proposed [19]. Apart from the use of MFM probes, all these methods lack the ability to control motion in two dimensions on magnetic surfaces.

It is known that skyrmions may be created and annihilated optically using laser pulses [20–23]. For all-optical control, a missing element is the ability to move magnetic skyrmions using laser beams. For magnetoelectric materials it has been proposed that multiferroic skyrmions may be manipulated using the electric field from a laser beam [24], and an inhomogeneous electric torque could be used to drive skyrmions in multiferroic or magnetic insulators [25]. Here it is proposed that laser beams may also be used to manipulate ferromagnetic and antiferromagnetic skyrmions, relying on the magnetoelastic (ME) effect due to thermoelastic lattice expansion, as well as local temperature gradients. The effect of temperature gradients on skyrmions has been discussed [26]. Anisotropy gradients, in particular, have been shown to generate skyrmion motion [27], with nanopatterning of the anisotropy landscape used to guide current-induced skyrmion motion [28], and entropic forces due to temperature gradients generate skyrmion Seebeck and Nernst effects [29]. Apart from forces arising directly from temperature gradients, a useful effect, which has not been discussed so far in the context of skyrmion motion, is thermoelastic lattice expansion resulting in a strain-induced magnetic anisotropy modification. Thermoelastic lattice expansion can be helpful, for example it can result in an enhanced magnonic spin Seebeck effect [30], and can even induce magnetization dynamics and spin currents in magnetic insulators [31]. Moreover, it is inextricably linked to temperature gradients, resulting

*slepadatu@uclan.ac.uk

in a magnetothermoelastic coupling effect, and a key message in this work is that an additional force due to lattice expansion arises on skyrmions, which must be taken into consideration.

From a practical perspective for potential applications, heat-assisted magnetic recording [32] already uses laser beams to control the magnetic anisotropy, relying on rapid spot heating approaching the Curie temperature. For all-optical magnetic skyrmion motion, it is shown here that spot heating up to 350 K is sufficient. Moreover, it is possible to generate and control on-chip laser beams, for example, using a MEMS steering system, achieving 3.3-μm diameter focused beam with steering speeds of 10 m/s over a travel distance of 10 μm [33], or using MEMS-controllable vertical-cavity surface-emitting laser (VCSEL) microlens arrays [34], with more recent efforts demonstrating MEMS-VCSEL multi-MHz rastering capability [35].

II. MAGNETOTHERMOELASTIC MODEL

The model is based on three coupled dynamics equations for magnetization, temperature, and elasticity properties:

$$\begin{aligned} \frac{\partial \mathbf{m}}{\partial t} &= -\gamma \mathbf{m} \times \mathbf{H}_{\text{eff}} + \alpha \mathbf{m} \times \frac{\partial \mathbf{m}}{\partial t}, \\ C\rho \frac{\partial T}{\partial t} &= K\nabla^2 T + S, \\ \rho \frac{\partial v_p}{\partial t} &= \sum_{q=x,y,z} \frac{\partial \sigma_{pq}}{\partial q} - \eta v_p, \ (p = x,y,z). \end{aligned} \tag{1}$$

The first equation is the Landau-Lifshitz-Gilbert (LLG) equation, where $\mathbf{m}$ is the magnetization direction, γ is the gyromagnetic ratio, and α is the Gilbert damping factor [36]. Here $\mathbf{H}_{\text{eff}}$ is a total effective field, which includes (i) demagnetizing field [37], (ii) uniaxial magnetocrystalline anisotropy, $\mathbf{H} = 2K_U(\mathbf{m} \cdot \mathbf{e}_A)\mathbf{e}_A/\mu_0 M_S$, where K_U is the uniaxial anisotropy constant, M_S is the saturation magnetization, and $\mathbf{e}_A = \hat{\mathbf{z}}$ is the easy-axis direction perpendicular to the plane, (iii) direct exchange interaction, $\mathbf{H} = 2A\nabla^2\mathbf{m}/\mu_0 M_S$, where A is the exchange stiffness constant, (iv) interfacial DMI, $\mathbf{H} = 2D((\nabla \cdot \mathbf{m})\hat{\mathbf{z}} - \nabla m_z)/\mu_0 M_S$, where D is the DMI constant, (v) external field, and (vi) ME interaction. Thus the LLG equation is coupled to the heat and elastodynamics equations through the temperature dependence of magnetic parameters, and through the ME interaction, respectively. The latter is due to spin-orbit interaction and has the energy density expression (ME field obtained as $\mathbf{H} = -(\partial E_{\text{ME}}/\partial \mathbf{m})/\mu_0 M_S$):

$$\begin{aligned} E_{\text{ME}} = {} & B_1[{m_x}^2\varepsilon_{xx} + {m_y}^2\varepsilon_{yy} + {m_z}^2\varepsilon_{zz}] \\ & + 2B_2[m_x m_y \varepsilon_{xy} + m_x m_z \varepsilon_{xz} + m_y m_z \varepsilon_{yz}]. \end{aligned} \tag{2}$$

Here B_1 and B_2 are ME coupling coefficients, and ε is the symmetric strain tensor with indicated linear and shear strain components. The magnetothermoelastic model is also applied here to antiferromagnetic skyrmions using the two-sublattice formulation [23]. Thus, the above expressions for magnetization and effective fields are applied separately to sublattices A and B, where $\mathbf{m}_i$ and $\mathbf{H}_i$ ($i = A, B$) are magnetization and field values respectively, on the two sublattices. Material parameter values are the same on the two sublattices, which are additionally coupled antiferromagnetically using a homogeneous exchange contribution with effective field $\mathbf{H}_{i,h} = -4A_h\mathbf{m}_i \times (\mathbf{m}_i \times \mathbf{m}_j)/\mu_0 M_S$, and nonhomogeneous exchange contribution with effective field $\mathbf{H}_{i,nh} = A_{nh}\nabla^2\mathbf{m}_j/\mu_0 M_S$ ($i,j = A, B, i \neq j$). Equation (1) gives the heat equation, where C is the specific heat capacity, ρ is the mass density, K is the thermal conductivity, T is the temperature, and S is a heat source. Here the heat source is due to a laser beam spot with Gaussian profile $S = S_0 exp(-2r^2/r_0^2)$, where r is the radial distance from the spot center, S_0 is the laser-beam power density, and $2r_0$ is the diffraction-limited spot size. On the one hand, the temperature increase gives rise to a temperature dependence of magnetic parameters, namely the magnetization length is scaled according to the Curie-Weiss law [38], $m_e(T) = B(m_e 3T_C/T)$, where B is the Langevin function and T_C is the Curie temperature. The uniaxial magnetocrystalline anisotropy constant is scaled as m_e^3 [39], the exchange stiffness and DMI constant are scaled as m_e^2 [40, 41]. Finally, the damping constant is scaled as $(1 - T/3T_C)$ [38]. On the other hand, the temperature increase gives rise to a mechanical stress in the elastodynamics equation, due to the thermoelastic effect. This is given in Eq. (1), written in the velocity-stress representation [42], where v is the velocity, σ is the symmetric stress tensor, and η is a mechanical damping factor resulting in energy dissipation. This is solved using the finite-difference time-domain (FDTD) scheme, with implementation details for the three-dimensional (3D) elastodynamics equation in multilayered structures given in Appendix A. The stress and strain for a cubic crystal are related using

$$\begin{aligned} \sigma_{pp} = {} & c_{11}\varepsilon_{pp} + c_{12}(\varepsilon_{qq} + \varepsilon_{ll}) - (c_{11} + 2c_{12})\alpha_T(T - T_0) \\ & + B_1 m_p^2, (p,q,l = x,y,z, \ p \neq q \neq l), \\ \sigma_{pq} = {} & 2c_{44}\varepsilon_{pq} + B_2 m_p m_q, \ (p,q = x,y,z, \ p \neq q). \end{aligned} \tag{3}$$

Here c_{11}, c_{12}, c_{44} are elastic stiffness coefficients (taken as $c_{11} = 300$ GN/m^2, $c_{12} = 200$ GN/m^2, and $c_{44} = 50$ GN/m^2 [43]), α_T is the linear thermal expansion coefficient, and in this work T_0 is the ambient temperature taken as 300 K. The terms involving B_1 and B_2 in Eq. (3) give the magnetostriction contribution. For use in Eq. (2), the strain is obtained by inverting Eq. (3). Note, the inverse thermoelastic effect (change in temperature due to lattice strains) is

not considered since it is negligible for the problem studied here.

Figure 1 shows the effect of a laser beam with spot size 0.8 μm (e.g., possible using a laser wavelength of 442 nm [44]) and $S_0 = 2.25 \times 10^{18}$ W/m^3. Energy is absorbed in the FM layer of thickness $t_{\rm FM} = 2$ nm, and integrating the laser-spot Gaussian profile gives the total power $P = S_0 t_{\rm FM} r_0^2 \pi (1 - e^{-2})/2 \cong 1$ mW. The actual laser power required to produce this depends on the material-specific laser-absorption coefficient, thus here we simply state the total absorbed power as used in computations. The structure used is a FM/HM bilayer track hosting Néel skyrmions (e.g., Co/Pt, where $A = 10$ pJ/m, and $D = -1$ mJ/m^2 [12], although the general physical picture presented here is not restricted to these materials), with FM thickness $t_{\rm FM} = 2$ nm, HM thickness $t_{\rm HM} = 30$ nm, width 0.4 μm, and length 2 μm. Further computational details are given in Appendix A. The laser beam is scanned along the track, through the center, with a set velocity (20 m/s used here) as indicated in Fig. 1(a), resulting in skyrmion motion due to attractive forces towards the center of the laser spot. Figure 1(b) shows the dynamic temperature profile half-way through the scan, with the maximum temperature increase of approximately 50 K reached at the center of the laser spot, decreasing either side. The trailing side has a higher temperature compared to the leading side due to finite heat dissipation time (heat is transferred to the surroundings according to Newton's law of cooling, implemented using Robin's boundary conditions [45]). A substrate is not included here for simplicity, although inclusion of a substrate material would result in a slightly larger temperature increase for the same heat-source power density [45]. The temperature profile gives rise to an effective anisotropy gradient since magnetic parameters have a temperature dependence, where $K_{\rm eff}(T) = m_e^2 (K_U m_e - \mu_0 M_S^2/2)$ is the effective anisotropy, decreasing towards the center of the laser spot. Here $K_U = 380$ kJ/m^3, $M_S = 600$ kA/m [12], and the Curie temperature is taken as 700 K. Anisotropy gradients result in a force on skyrmions [27], and in this case we have a force acting towards the center of the laser spot, $F_{\rm TG}$, as indicated in Fig. 1(b). This is further enhanced due to the increase in skyrmion diameter with decreasing anisotropy, which is known to accelerate skyrmion motion [27]. It should also be noted that the decrease in $A(T)$ and $D(T)$ with temperature has a net opposite effect here (also see Ref. [26]), as the net increase in skyrmion diameter with temperature is reduced, however for the parameter values and their temperature dependences used here, the net effect of $F_{\rm TG}$ is to cause movement towards the hotter laser-spot center. On the other hand, the temperature increase results in sample strains due to the thermoelastic effect, with the ε_{zz} strain component shown in Fig. 1(c), where the bottom face of the HM layer is mechanically fixed (e.g., as would result when in contact with a stiff substrate). Here $\alpha_T = 10^{-5}$ K^{-1} is taken as a typical order-of-magnitude linear thermal expansion coefficient in thin metallic films (e.g., for ultrathin Co/Pt bilayers see Ref. [46]). The resulting strain is of the order 10^{-3}, which generates a significant ME effect. The ME coupling energy density is shown in Eq. (2), proportional to the ME coupling coefficient $B_1 = 10$ MJ/m^3 (e.g., this value is used to explain the effect of SAWs on skyrmion creation in Co/Pt/Ir tracks [16]). Here we also set $B_2 = B_1$, although the ME effect on skyrmions due to shear strains is negligible here. With a positive ME coupling, a tensile strain as in Fig. 1(c) induces a hard magnetic axis, and easy-plane perpendicular to the strain. Thus the ME effect is an useful additional source of magnetic anisotropy, resulting in an anisotropy gradient and an additional force on skyrmions, $F_{\rm ME}$, which for positive ME coupling also acts towards the center of the laser spot.

III. ISOLATED SKYRMION MOTION IN MAGNETIC TRACKS

Skyrmion motion in magnetic tracks is now investigated in more detail. A useful model to understand skyrmion motion is the Thiele equation, derived from the LLG equation under simplifying assumptions [47], and extended more recently to include acceleration effects in a linear anisotropy gradient [27]:

$$\mathbf{G} \times \mathbf{v} + \alpha \mathbf{D} v = -\nabla U. \tag{4}$$

Here $\mathbf{G} = -4\pi Q \hat{z}$ is the gyrovector, where $Q = \int \mathbf{m} \cdot (\partial \mathbf{m}/\partial x \times \partial \mathbf{m}/\partial y) dx dy/4\pi$ is the topological number with the integral taken over the magnetic surface, and for ferromagnetic skyrmions we have $Q = \pm 1$. In Eq. (4) $\mathbf{v}$ is the skyrmion velocity, $\alpha \mathbf{D} v$ is a dissipative term proportional to the Gilbert-damping parameter α (here we set $\alpha = 0.1$ [48]), where $\mathbf{D}$ is the dissipative tensor dependent on the skyrmion structure, and $\mathbf{F} = -\nabla U$ is the driving force obtained as the gradient of the potential energy. Thus, for objects with nonzero topological number, the velocity is not along the driving-force direction, but acquires an orthogonal component reminiscent of the Magnus effect. As discussed above, the driving forces are $F_{\rm TG}$ and $F_{\rm ME}$, obtained from material parameter gradients due to temperature gradients, including effective anisotropy gradients, and strain-induced anisotropy gradients, respectively. These are computed in Ref. [49] as a function of power, e.g., for $P = 1$ mW, we have 23.8 and 28.4 GN/m^3 maximum gradient magnitudes for $F_{\rm TG}$ and $F_{\rm ME}$, respectively.

Thus it is expected that the force, due to ME coupling, has a stronger effect than that due to thermal gradients in the case investigated here. Although this depends on the particular material parameters, the key message is the ME effect, as a result of thermoelastic lattice expansion, has an important contribution, and it is not sufficient to consider

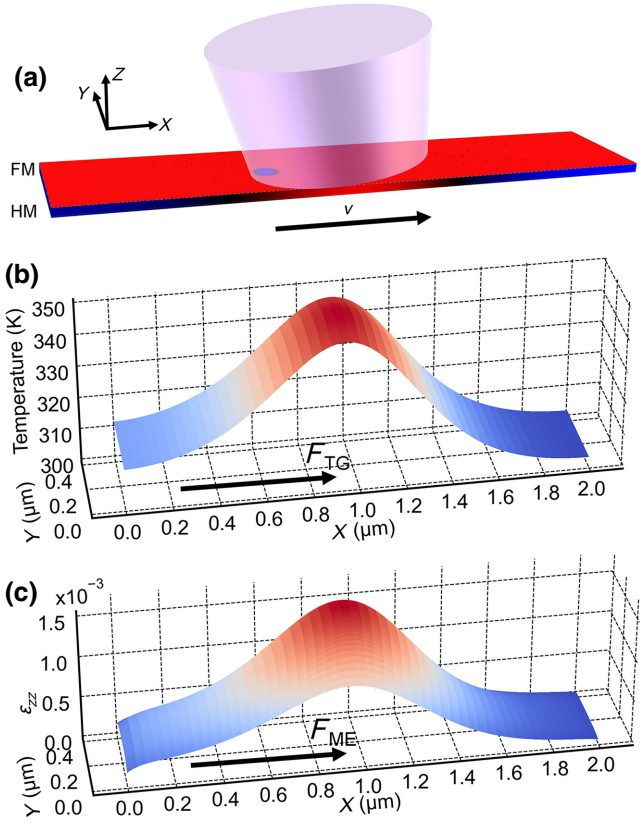

FIG. 1. Skyrmion motion generated by scanning a focused laser beam, due to magnetothermoelastic coupling in a magnetic track. (a) Magnetic track showing a skyrmion being moved using a focused laser beam (1-mW absorbed power) and with a set velocity along the track ($v = 20$ m/s). In the FM layer, red indicates magnetization out of the plane, and blue into the plane. (b) Computed dynamic temperature profile. A force towards the center of the laser spot arises directly due to temperature gradients, F_{TG}. (c) Computed z-direction dynamic strain profile. A strain-induced graduated magnetic anisotropy is generated, which for positive ME coupling results in an additional force towards the center of the laser spot, F_{ME}.

only the force due to temperature gradients. Examples of computed skyrmion paths for the track considered above are shown in Fig. 2(a), obtained for $P = 1$ mW and laser-spot velocity of 5 m/s, where the laser spot starts at $x = 0.3$ μm and terminates at $x = 1.7$ μm. To see the separate effects of F_{TG} and F_{ME}, computations are performed as follows: (i) ME coupling disabled, thus F_{ME} becomes zero, and (ii) ME coupling enabled, however the temperature dependence of magnetic parameters is kept constant for $T > 300$ K, and thus F_{TG} becomes zero. These two separate cases are shown in Fig. 2(a) as (i) dashed-dot and (ii) dashed lines, respectively, where an out-of-plane magnetic field of 10 kA/m is used to stabilize a Néel skyrmion with 35-nm starting diameter. The Magnus effect is significant, resulting in a skyrmion velocity component perpendicular to the anisotropy gradient, with sign dependent on the topological number as expected. The computation is also repeated for antiferromagnetic skyrmions ($Q = 0$), and as expected the Magnus effect vanishes, with the skyrmion following the laser spot in a straight line. For $Q = 0$ no out-of-plane magnetic field is used, however $D = -2.5$ mJ/m^2 in order to stabilize an antiferromagnetic skyrmion also with 35-nm starting diameter; all other magnetic parameters are the same, applied equally to the two sublattices, and additionally the homogeneous and nonhomogeneous antiferromagnetic exchange contributions have parameters $A_h = 10$ pJ/m and $A_{nh} = -10$ MJ/m^3, respectively. It is also observed that the effect of F_{ME} is stronger than that of F_{TG} as expected—indeed, with F_{TG} alone the skyrmion is not displaced for the full laser-spot travel distance, but loses tracking half-way through the scan. The full, combined effect, is shown using solid lines in Fig. 2. It is observed the skyrmion undergoes an incomplete *bouncing orbit* motion, before settling into an off-center dynamic equilibrium position. As shown in Ref. [50], the effect of anisotropy gradients, both for ferromagnetic and antiferromagnetic skyrmions, is to induce motion towards the region of lowest anisotropy. The results shown here are in agreement, with both F_{TG} and F_{ME} causing skyrmion motion towards the region of lowest anisotropy. It is also known that skyrmions interact with track edges with a repulsive force [51,52], and this is also the case here. Whilst the skyrmion Hall effect does not prevent motion along the laser-spot movement direction, for weaker driving forces the skyrmion can get close to the edge of the track, as seen in Fig. 2(a) for the case with F_{TG} only where motion is confined along the track edge. Further information is obtained by investigating the skyrmion velocity as a function of time, shown in Fig. 2(b). For $|Q| = 1$ it is observed that the skyrmion undergoes large, damped velocity oscillations for the first 150 ns, before settling into the steady state 5-m/s forward velocity. Whilst an off-center dynamic equilibrium position is reached in the steady state, displacement away from this equilibrium position causes additional restoring forces, and thus an acceleration, which results in a transient velocity response initially exceeding the constant 5-m/s laser-spot velocity. For the same power of 1 mW, for $Q = 0$ the skyrmion also undergoes an initial acceleration in the first 50 ns, before settling into the steady-state velocity of 5 m/s.

Before investigating the effect of varying beam power and velocity, it is worthwhile to discuss the effect due to the sign of ME coupling coefficient, B_1. Both negative and positive values are possible [53]. Positive ME coupling coefficients have been obtained in skyrmion-supporting MnSi [54–56], whilst positive effective ME coupling in ultrathin Fe films was measured due to different contributions of bulk and surface ME contributions [57]. The ME coupling also depends on the lattice parameter [58], and large positive ME coupling in thin Fe films was measured [59], which was found to change sign and become

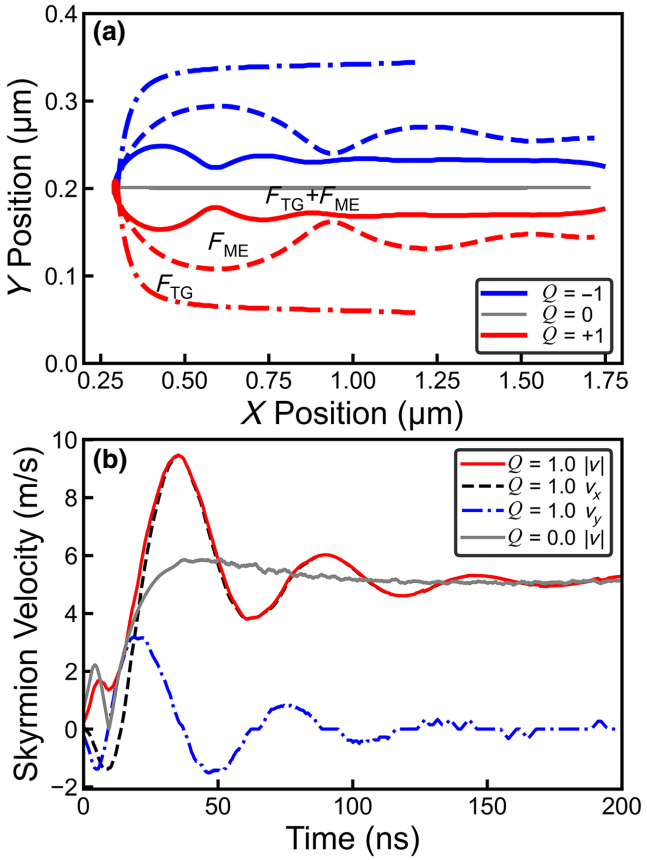

FIG. 2. (a) Computed skyrmion paths for 1-mW absorbed power, with laser spot scanned at 5 m/s through the center of a track 400 nm wide and 2 μm long, shown for ferromagnetic skyrmions ($Q=\pm1$) and antiferromagnetic skyrmion ($Q=0$). The dash-dot lines show the skyrmion motion without the ME effect, with the resultant motion dependent on the force arising from temperature gradients, F_{TG}, and the effective force due to the Magnus effect, given by the gyrovector term contribution in Eq. (4), $\mathbf{G}\times\mathbf{v}$. The dashed lines show the skyrmion motion due to the ME effect, F_{ME}, with magnetic parameter temperature dependences disabled. The solid lines show the combined effect, noting that for $Q=0$ there is no net Magnus force. (b) Skyrmion velocities, showing the velocity magnitude as well as the x and y components. The steady-state target velocity of 5 m/s is reached following an initial damped oscillatory response, particularly pronounced for $Q\neq0$ where the Magnus force contributes.

negative for thicker Fe films. For thin Ni films, positive ME coupling was also measured, with sign dependent on film thickness [60]. For hcp Co large positive values exceeding 10 MJ/m^3 have also been measured [61]. Moreover, a value of $B_1=10$ MJ/m^3 was used to explain the effect of SAWs on magnetic skyrmions in Pt/Co/Ir tracks [16]. If B_1 is negative the sign of F_{ME} is reversed, and thus opposes F_{TG}. In this case, a tensile strain induces an easy axis, and a hard plane perpendicular to the strain axis, with the strain-induced magnetic anisotropy gradient of opposite sign. As shown in Ref. [49], indeed the effect of F_{ME} alone for $B_1=-10$ MJ/m^3 is to cause skyrmion motion away from the laser-spot center, although the effect is reduced since the skyrmion diameter is also reduced as the total anisotropy increases. The dissipative term in the Thiele equation, $\alpha\mathbf{D}v$, is dependent on the skyrmion diameter, resulting in smaller velocities for smaller diameters. The combination of F_{ME} and F_{TG} nearly cancels out due to opposite directions, on the one hand, with the effect on skyrmion motion also reduced due to reduction in skyrmion diameter. Conversely, when the ME coupling is positive, the combined effect of F_{ME} and F_{TG} is enhanced as the skyrmion diameter increases due to decreasing total anisotropy—the skyrmion diameter in this case, as a function of power, is also shown in Ref. [49], which reaches approximately 120 nm at 1-mW power. In terms of maximizing the effect of F_{ME} for potential applications, a few criteria may be identified. As discussed above, materials with large, and positive, magnetoelastic coupling are required. It is also proportional to the generated strain, and thus proportional to the thermoelastic coefficient of the material and temperature change. However, the generated strain also depends on the coefficients of elastic stiffness, and specifically on the Poisson ratio, $c_{12}/(c_{11}+c_{12})$. The thermoelastic effect causes lattice expansion not only in the out-of-plane direction, but also in the plane. Thus materials with a large Poisson ratio are also desirable here, in order to maximize the perpendicular strain, and therefore F_{ME}.

Increasing the power results in stronger forces, as the maximum temperature, perpendicular strain, and therefore anisotropy gradient magnitudes increase (see Ref. [49] for details). Thus it is expected that larger powers allow the skyrmion to be moved with larger velocities. This is shown in Fig. 3 both for ferromagnetic ($|Q|=1$), and antiferromagnetic skyrmions ($Q=0$). Here the skyrmion path is computed as a function of power and laser beam velocity, with the total skyrmion displacement shown normalized to the laser-spot travel distance. If the power is insufficient for a given beam velocity, then skyrmion tracking is lost, which defines region IIb in Fig. 3. The boundary delimiting this region is shown, obtained by fitting a logistic function to the normalized skyrmion displacement, $d_{Sk}=1/(1+e^{-(P-P_0)/w})$ with transition region width w and threshold power P_0. Above this threshold the skyrmion is displaced without losing track of the laser spot, which defines region I. At higher powers, it is helpful to make a distinction however, since the local reduction in total anisotropy results in unstable skyrmions, which are dynamically distorted into *skyrmion strings* (see Ref. [49] for an example), defining region IIa. Comparing thresholds for ferromagnetic and antiferromagnetic skyrmions, it is seen that for $Q=0$ larger powers are required to fully displace the skyrmion, and also the boundary separating regions I and IIa is shifted up. This is largely because the demagnetizing field is negligible, resulting in a weaker dependence of skyrmion diameter on temperature (see Ref. [49]). At even higher

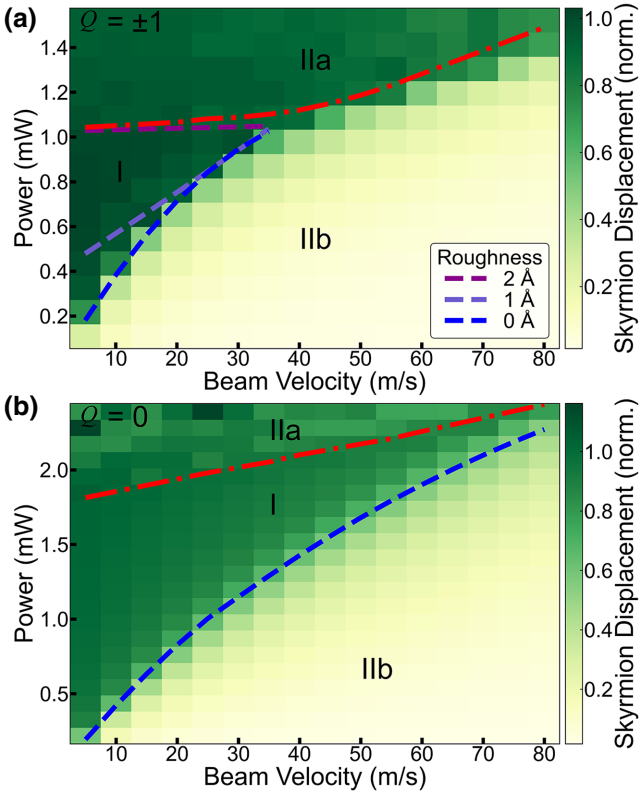

FIG. 3. Skyrmion displacement (normalized to laser-spot travel distance) as a function of power- and laser-beam velocity, for (a) ferromagnetic skyrmion, and (b) antiferromagnetic skyrmion. Three regions are distinguished: in region I the skyrmion is displaced for the full laser-spot travel distance without distortion, in region IIb the power is insufficient to fully displace the skyrmion, and travels only a fraction of the laser-spot travel distance, and in region IIa, at larger powers, the skyrmion is dynamically distorted into a *skyrmion string*. Region IIb lies below the dashed line, region I lies above the dashed line and below the dash-dot line, while region IIa lies above the dash-dot line. For the ferromagnetic skyrmion, results with different amplitudes of surface roughness, 0 Å (perfect surface), 1 Å, and 2 Å, are shown.

powers it is possible to nucleate skyrmions, which is another useful aspect for all-optical devices, although this typically requires pulses [22] rather than a continuous beam as used here.

Finally, the effect of landscape disorder is briefly addressed. For current-induced skyrmion motion it is known that disorder results in increased threshold current densities, reduced velocities and a variation of the skyrmion Hall angle with velocity [62–64]. Moreover, defects also affect antiferromagnetic skyrmions [65]. Here landscape disorder is introduced in the form of surface roughness [64] using an effective field model developed previously [66], considering cases with 1- and 2-Å roughness amplitude, and in-plane correlation length of 40 nm. As shown in Fig. 3(a), increasing the roughness amplitude results in a shift of the threshold boundary separating regions IIb and I to higher powers. This is expected since larger forces are required to depin skyrmions from pinning potentials formed by the landscape disorder. These results demonstrate that all-optical skyrmion motion, using the magnetothermoelastic coupling mechanism, is feasible even when sample imperfections are present, although as the case with 2-Å roughness amplitude shows, excessive imperfections can be problematic for achieving distortion-free skyrmion displacement. It is also known that thermal effects contribute to skyrmion motion under temperature gradients, resulting in diffusion, thermal activation, and entropic forces [67]. Whilst the key messages in this work remain, namely skyrmions may be moved all optically using a focused laser spot, and thermoelastic lattice expansion due to temperature gradients results in a magnetoelastic force on skyrmions, the current model may be extended to include stochastic thermal effects, however this is reserved for a future work.

IV. DIRECTED SKYRMION MOTION

One key advantage the all-optical skyrmion motion mechanism presented here has over conventional current-induced skyrmion motion, and even SAW-induced skyrmion motion, is the ability to controllably move skyrmions on magnetic surfaces in any direction. An example of directed skyrmion motion is shown in Fig. 4, where a magnetic surface of 2×2 μm^2 is used, and the laser spot is rotated about the center with a 700-nm radial distance. The starting position for the skyrmion and laser spot are $x = 1.7$ μm, $y = 1$ μm as indicated in Fig. 4, and two cases are investigated for clockwise and anticlockwise laser-spot paths. Using a power of 1 mW and linear velocity of 5 m/s, in both cases the skyrmion is observed to track the laser spot fully. For a topological charge $Q = -1$ the skyrmion has a spiralling clockwise orbit motion around the laser-spot center (see Ref. [49]). Thus, for a laser spot moving in a clockwise path, the skyrmion begins moving towards the outside of the circle traced by the laser. In this case, the skyrmion is always found on the outside of the circular path traced by the laser. On the other hand, for a laser spot moving in an anticlockwise path, the skyrmion starts moving towards the inside of the circle traced by the laser, in order to maintain its clockwise orbit direction. In this case, the skyrmion is always found on the inside of the circle traced by the laser. This results in a smaller average distance from the laser spot, since for an anticlockwise laser-spot movement direction, the skyrmion path always curves towards the circular laser path, whilst for a clockwise laser-spot movement direction, the skyrmion path curves away from the circular laser path. Unlike the case of magnetic tracks, it is expected that the two movement directions now have different power thresholds for any

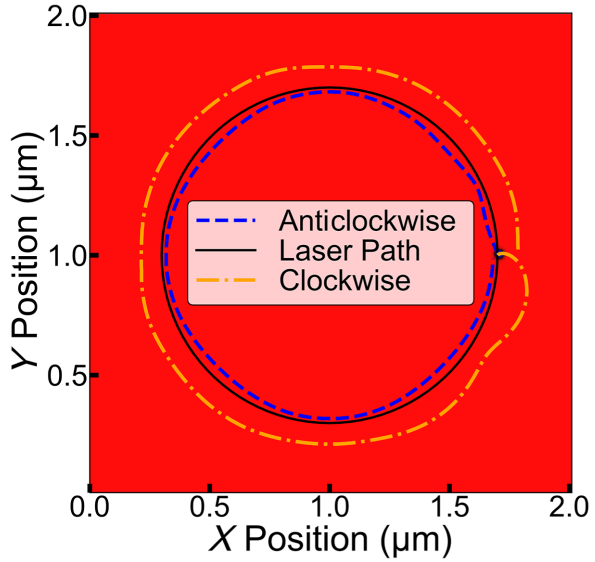

FIG. 4. Directed skyrmion ($Q=-1$) motion due to a circular laser path, with 1-mW power and 5-m/s tangential velocity (period of 880 ns). The plotted skyrmion paths are computed for clockwise and anticlockwise laser-path directions.

given beam velocity. Investigation of power thresholds for curved ferromagnetic skyrmion motion however is outside the scope of the current work, and the results shown in Fig. 4 demonstrate the possibility to guide skyrmions in any direction on a magnetic surface. Circular skyrmion motion is also obtained in spin-torque nano-oscillators, both for ferromagnetic and antiferromagnetic skyrmions [68,69]. The all-optical method presented here is an alternative to using electrical currents. Here, an oscillating laser spot can be used to tune the oscillation frequency, as well as the radial position independently, obtaining an all-optical skyrmion-based nano-oscillator.

V. EFFECT ON SKYRMION LATTICES

It is also possible to address multiple skyrmions using a single laser spot, and this is discussed for a skyrmion lattice. Moreover, for experimental verification of the all-optical control mechanism presented here, it is advantageous to first investigate a simple case where the beam is stationary. A suggested case is shown in Fig. 5(a), where a simple 2×2 μm^2 square is used, hosting a ferromagnetic skyrmion lattice configuration. A stationary laser spot is centered on the sample, and computed skyrmion paths are plotted in Fig. 5, with the initial skyrmion lattice configuration shown. The same forces discussed in previous sections are present, however we also have additional repulsive interactions between skyrmions. Thus the central skyrmion is stabilized at the laser-spot center, however the neighboring skyrmions undergo a clockwise orbiting motion due to the Magnus effect ($Q=-1$). Skyrmions are attracted to the center due to the combination of F_{TG} and F_{ME}, with the effect decreasing away from the laser spot. Since the orbiting skyrmions are prevented from spiralling all the way towards the laser-spot center, owing to repulsive interactions with skyrmions closer or at the center [52], the net effect is an orbiting motion for the entire lattice. Thus an experimental verification here could consist of observing the rotation of a skyrmion lattice using a suitable direct imaging technique, before and after application of a focused laser pulse of sufficiently large power and small spot size.

A further example is given in Fig. 5(b), where the effect of a moving laser spot, with 10 m/s velocity, on a skyrmion lattice is shown. Skyrmions tend to rotate clockwise due to the Magnus force, however skyrmions in the top-right part acquire an overall anticlockwise rotation due to repulsive interactions with skyrmions originating from the lower half. The effect is a net accumulation of

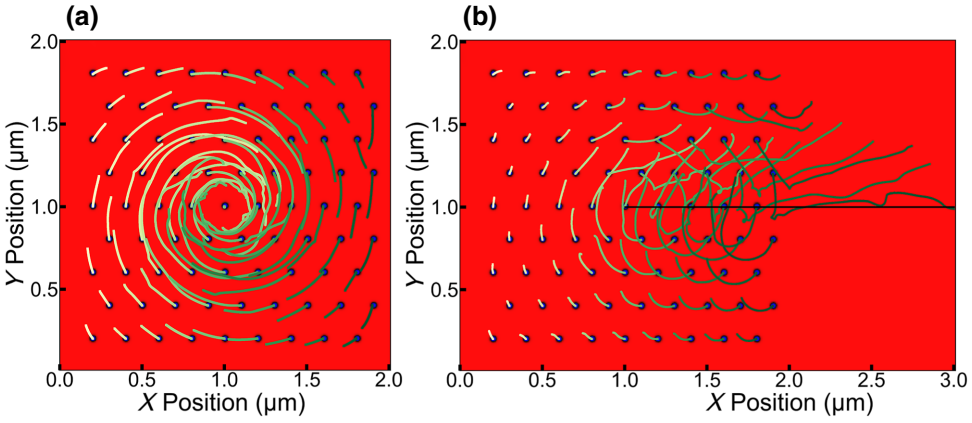

FIG. 5. Effect of a laser spot on a skyrmion lattice (skyrmions with $Q=-1$). Initial positions are shown, with overlaid computed paths in response to a laser spot with 1.5-mW power. (a) Laser spot is static and centered, and skyrmions rotate clockwise due to the Magnus force, with effect increasing closer to the center; the skyrmion at the center provides a repulsive force on neighboring skyrmions. (b) The laser spot moves with velocity of 10 m/s along the black horizontal line. A net accumulation of skyrmions in the upper-half results.

skyrmions in the top half. Thus, unlike the static laser-spot case, due to the incomplete orbiting motion as the laser spot moves, a symmetry-breaking effect is generated, where a net accumulation of skyrmions is obtained in the top half. Reversing the beam travel direction results in a net accumulation of skyrmions in the bottom half. Further work is required to fully investigate the effect of magnetothermoelastic coupling on skyrmion lattices, and it is hoped the present work will stimulate efforts in this direction.

VI. CONCLUSIONS

For magnetic thin films hosting skyrmions, using a focused laser beam to produce a local temperature gradient, and hence a thermoelastic lattice expansion, it was shown that forces are generated due to magnetothermoelastic coupling. One such force is due to magnetic parameter gradients, especially local effective anisotropy gradients generated by local temperature gradients, acting towards the center of the laser spot. Another equally useful force however, is due to the ME effect as a result of thermoelastic lattice expansion, and it was shown that for positive ME coupling coefficients this force also acts towards the center of the laser spot, with the two effects reinforcing each other owing to an increase in skyrmion diameter. Conversely, for negative ME coupling coefficients, the two forces nearly cancel out, largely due to their opposing directions. By moving the laser spot, ferromagnetic and antiferromagnetic skyrmion displacement is shown, with a threshold power dependent on the beam velocity. This method of all-optically generated skyrmion displacement allows full control of motion over two-dimensional magnetic surfaces, with a possible method of MEMS-VCSEL on-chip integration discussed in the introduction, in contrast to current-induced skyrmion motion, or even SAW-generated skyrmion motion, which are limited by lithographically defined electrodes. It is hoped this work will stimulate future efforts in this direction, with methods of experimental verification also discussed, particularly for skyrmion lattices. Further possible extensions include use of synthetic antiferromagnetic multilayers, where the skyrmion Hall effect vanishes [70], but also combined current and focused laser pulse control to achieve skyrmion motion gating and controlled deflection.

APPENDIX A

The magnetothermoelastic model is implemented in BORIS [71] using finite differences, running on CUDA-enabled graphical processing units. The strain is related to mechanical displacement, **u**, as

$$\varepsilon_{pq} = \frac{1}{2}\left(\frac{\partial u_p}{\partial q} + \frac{\partial u_q}{\partial p}\right),\ (p,q = x,y,z). \tag{A1}$$

Taking the time derivative of Eqs. (3) and (A1) allows replacing the displacement with velocity, and together with Eq. (1) we obtain a system of first-order differential equations for elastodynamics, written in the velocity-stress representation as

$$\begin{aligned}
\rho\frac{\partial v_p}{\partial t} &= \sum_{q=x,y,z}\frac{\partial \sigma_{pq}}{\partial q} - \eta v_p,\ (p = x,y,z),\\
\frac{\partial \sigma_{pp}}{\partial t} &= c_{11}\frac{\partial v_p}{\partial p} + c_{12}\left(\frac{\partial v_q}{\partial q} + \frac{\partial v_l}{\partial r}\right) - (c_{11}+2c_{12})\alpha_T\frac{\partial T}{\partial t}\\
&\quad + 2B_1 m_p\frac{\partial m_p}{\partial t},\ (p,q,l = x,y,z,\ p \neq q \neq l),\\
\frac{\partial \sigma_{pq}}{\partial t} &= c_{44}\left(\frac{\partial v_p}{\partial q} + \frac{\partial v_q}{\partial p}\right) + B_2\left(m_p\frac{\partial m_q}{\partial t} + m_q\frac{\partial m_p}{\partial t}\right),\\
&\quad (p,q = x,y,z,\ p \neq q).
\end{aligned} \tag{A2}$$

Time derivatives of temperature and magnetization, necessary for Eq. (A2), are evaluated directly from Eq. (1).

The equations are solved using the FDTD scheme, with staggered velocity and stress components as indicated in Fig. 6 for a given computational cell. The temperature and magnetization values are cell centered; their values and that of their time derivative at vertices, edge, and face centers, are obtained to second-order accuracy in space using interpolation. Spatial derivatives at inner points are evaluated using standard finite differences to second-order accuracy [72]. There must be at least one fixed surface where the mechanical displacement is zero, since no translational motion is allowed, and thus the velocity is also zero. Velocity components on a fixed surface are set directly as zero, whilst derivatives of velocity components perpendicular to a fixed surface are evaluated using standard expressions with Dirichlet boundary condition of zero [72]. As an example, for a fixed xz surface in Fig. 6, $v_x = v_z = 0$, whilst for $\partial v_y/\partial y$ at the boundary the Dirichlet condition $v_y = 0$ applies. For all other surfaces (free surfaces) boundary stress values are prescribed from external forces as (δ is the Kronecker δ):

$$\sum_{q=x,y,z}\sigma_{pq}\delta_{lq} = F_l,\ (p,l = x,y,z). \tag{A3}$$

For Eq. (A3) p is normal to the free surface. In this work there are no external forces, thus **F** is zero on all surfaces. The boundary stress values are either set directly for components on free surfaces, or else are used as Dirichlet boundary conditions to evaluate derivatives of stress perpendicular to a free surface. As an example, for a fixed xz surface in Fig. 6, $\sigma_{yy} = F_y$ is set directly, whilst $\sigma_{xy} = F_x$ and $\sigma_{yz} = F_z$ are used as Dirichlet boundary conditions to evaluate $\partial\sigma_{xy}/\partial y$ and $\partial\sigma_{yz}/\partial y$, respectively, at the boundary. Finally, required derivatives of velocity perpendicular

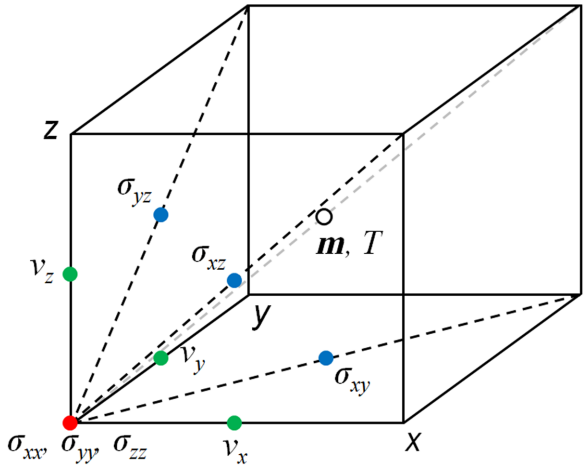

FIG. 6. Velocity, stress, magnetization, and temperature components for finite-difference discretization of the magnetothermoelastic model. Velocity components are edge centered, diagonal stress components are at vertices, shear stress components are face centered, and magnetization and temperature values are cell centered.

to a free surface are obtained from Eq. (A2), using boundary values for the time derivative of stress, in turn obtained from the time derivative of Eq. (A3) (also zero in this work). These are obtained in general as (p is normal to the free surface):

$$\frac{\partial v_p}{\partial p} = \frac{1}{c_{11}}\frac{\partial F_p}{\partial t} - \frac{c_{12}}{c_{11}}\left(\frac{\partial v_q}{\partial q} + \frac{\partial v_l}{\partial r}\right) + \left(1 + 2\frac{c_{12}}{c_{11}}\right)\alpha_T \frac{\partial T}{\partial t} - \frac{2B_1}{c_{11}} m_p \frac{\partial m_p}{\partial t}, \times (p, q, l = x, y, z,\ p \neq q \neq l). \tag{A4}$$

For multilayered structures, such as the FM/HM bilayer investigated here, composite media boundary (CMB) conditions are also required. Using the scheme in Fig. 6, these consist of enforcing continuity of velocity and stress components located on the CMB interface, achieved by interpolating respective values either side of the interface. These values are set after the elastodynamics equation is iterated in all layers. It is also necessary to specify initial values for stress and velocity. The velocity initial value is zero throughout, whilst the initial values of stress components, which are not on a free surface where Eq. (A3) applies, are computed using Eq. (3) by taking the initial strain to be zero.

The LLG equation is solved using the implemented RK4 method [73] with 200-fs time step, using the temperature and strain values available at the start of each time step. The heat equation is solved using the forward-time centered-space method with 100-fs time step. The elastodynamics equation is solved with velocity and stress staggered in time, i.e., velocity is updated first, and resulting values are used to update the stress using Eq. (A2). The time step for the elastodynamics equation is $\Delta t = 100$ fs, which satisfies the Courant, Friedrichs, Lewy condition, $\Delta t < 1/\left(v_p\sqrt{\Delta x^{-2} + \Delta y^{-2} + \Delta z^{-2}}\right)$, where v_p is the elastic compressional wave velocity ($v_p = 6000$ m/s here), and Δx, Δy, Δz are the cell-size dimensions. The FM layer is discretized as (4, 4, 1 nm) for the elastodynamics and heat equations, whilst the magnetic cell size is 2 nm. The HM layer is discretized as (4, 4, 5 nm) for the elastodynamics and heat equations. Finally, material values not specified in the main text are $C = 420$ J/kgK, $\rho = 8920$ kg/m^3, $K = 122$ W/mK for FM (bulk Co values), and $C = 125.6$ J/kgK, $\rho = 21\,452$ kg/m^3, $K = 71.6$ W/mK for HM (bulk Pt values). For both FM and HM the mechanical damping is $\eta = 10^{16}$ kg/m^{3}s, although this does not affect strain values obtained on the timescale of magnetization processes, and serves to absorb the much faster transient elastic waves.

[1] A. N. Bogdanov and D. A. Yablonsky, Thermodynamically stable "vortices" in magnetically ordered crystals. The mixed state of magnets, Sov. Phys. JETP **68**, 101 (1989).

[2] I. Dzyaloshinskii, A thermodynamic theory of 'weak' ferromagnetism of antiferromagnetics, J. Phys. Chem. Solids **4**, 241 (1958).

[3] T. Moriya, Anisotropic superexchange interaction and weak ferromagnetism, Phys. Rev. **120**, 91 (1960).

[4] X. Z. Yu, Y. Onose, N. Kanazawa, J. H. Park, J. H. Han, Y. Matsui, N. Nagaosa, and Y. Tokura, Real-space observation of a two-dimensional skyrmion crystal, Nature **465**, 901 (2010).

[5] C. Moreau-Luchaire, C. Moutafis, N. Reyren, J. Sampaio, C. A. F. Vaz, N. van Horne, K. Bouzehouane, K. Garcia, C. Deranlot, P. Warnicke, *et al.*, Additive interfacial chiral interaction in multilayers for stabilization of small individual skyrmions at room temperature, Nat. Nanotechnol. **11**, 444 (2016).

[6] K. M. Song, J.-S. Jeong, B. Pan, X. Zhang, J. Xia, S. Cha, T.-E. Park, K. Kim, S. Finizio, J. Raabe, *et al.*, Skyrmion-based artificial synapses for neuromorphic computing, Nat. Electron. **3**, 148 (2020).

[7] R. Chen, C. Li, Y. Li, J. J. Miles, G. Indiveri, S. Furber, V. F. Pavlidis, and C. Moutafis, Nanoscale Room-Temperature Multilayer Skyrmionic Synapse for Deep Spiking Neural Networks, Phys. Rev. Appl. **14**, 014096 (2020).

[8] R. Chen, Y. Li, V. F. Pavlidis, and C. Moutafis, Skyrmionic interconnect device, Phys. Rev. Res. **2**, 043312 (2020).

[9] D. Pinna, F. Abreu Araujo, J.-V. Kim, V. Cros, D. Querlioz, P. Bessiere, J. Droulez, and J. Grollier, Skyrmion Gas Manipulation for Probabilistic Computing, Phys. Rev. Appl. **9**, 064018 (2018).

[10] A. Fert, V. Cros, and J. Sampaio, Skyrmions on the track, Nat. Nanotechnol. **8**, 152 (2013).

[11] G. Yu, P. Upadhyaya, X. Li, W. Li, S. K. Kim, Y. Fan, K. L. Wong, Y. Tserkovnyak, P. K. Amiri, and K. L. Wang, Room-temperature creation and spin–orbit torque manipulation of skyrmions in thin films with engineered asymmetry, Nano Lett. **16**, 1981 (2016).

[12] S. Woo, K. Litzius, B. Krüger, M. Im, L. Caretta, K. Richter, M. Mann, A. Krone, R. M. Reeve, M. Weigand, *et al.*, Observation of room-temperature magnetic skyrmions and their current-driven dynamics in ultrathin metallic ferromagnets, Nat. Mater. **15**, 501 (2016).

[13] W. Jiang, X. Zhang, G. Yu, W. Zhang, X. Wang, M. B. Jungfleisch, J. E. Pearson, X. Cheng, O. Heinonen, K. L. Wang, *et al.*, Direct observation of the skyrmion Hall effect, Nat. Phys. **13**, 162 (2017).

[14] C. R. MacKinnon, S. Lepadatu, T. Mercer, and P. R. Bissell, Role of an additional interfacial spin-transfer torque for current-driven skyrmion dynamics in chiral magnetic layers, Phys. Rev. B **102**, 214408 (2020).

[15] S. Lepadatu, Effect of inter-layer spin diffusion on skyrmion motion in magnetic multilayers, Sci. Rep. **9**, 9592 (2019).

[16] T. Yokouchi, S. Sugimoto, B. Rana, S. Seki, N. Ogawa, S. Kasai, and Y. Otani, Creation of magnetic skyrmions by surface acoustic waves, Nat. Nanotechnol. **15**, 361 (2020).

[17] A. Casiraghi, H. Corte-León, M. Vafaee, F. Garcia-Sanchez, G. Durin, M. Pasquale, G. Jakob, M. Kläui, and O. Kazakova, Individual skyrmion manipulation by local magnetic field gradients, Commun. Phys. **2**, 145 (2019).

[18] Z. Wang, M. Guo, H.-A. Zhou, L. Zhao, T. Xu, R. Tomasello, H. Bai, Y. Dong, S.-G. Je, W. Chao, H.-S. Han, *et al.*, Thermal generation, manipulation and thermoelectric detection of skyrmions, Nat. Electron. **3**, 672 (2020).

[19] Y. Wang, T. Kitamura, J. Wang, H. Hirakata, and T. Shimada, Mechanical Acceleration and Control of the Thermal Motion of a Magnetic Skyrmion, Phys. Rev. Appl. **18**, 014049 (2022).

[20] K. Gerlinger, B. Pfau, F. Buttner, M. Schneider, L.-M. Kern, J. Fuchs, D. Engel, C. M. Gunther, M. Huang, I. Lemesh, *et al.*, Application concepts for ultrafast laser-induced skyrmion creation and annihilation, Appl. Phys. Lett. **118**, 192403 (2021).

[21] S.-G. Je, P. Vallobra, T. Srivastava, J.-C. Rojas-Sánchez, T. H. Pham, M. Hehn, G. Malinowski, C. Baraduc, S. Auffret, G. Gaudin, *et al.*, Creation of magnetic skyrmion bubble lattices by ultrafast laser in ultrathin films, Nano Lett. **18**, 7362 (2018).

[22] F. Büttner, B. Pfau, M. Böttcher, M. Schneider, G. Mercurio, C. M. Günther, P. Hessing, C. Klose, A. Wittmann, K. Gerlinger, *et al.*, Observation of fluctuation-mediated picosecond nucleation of a topological phase, Nat. Mater. **20**, 30 (2021).

[23] S. Lepadatu, Emergence of transient domain wall skyrmions after ultrafast demagnetization, Phys. Rev. B **102**, 094402 (2020).

[24] X.-G. Wang, L. Chotorlishvili, V. K. Dugaev, A. Ernst, I. V. Maznichenko, N. Arnold, C. Jia, J. Berakdar, I. Mertig, and J. Barnaś, The optical tweezer of skyrmions, Comput. Mater. **6**, 140 (2020).

[25] X.-G. Wang, L. Chotorlishvili, G.-H. Guo, C.-L. Jia, and J. Berakdar, Thermally assisted skyrmion drag in a nonuniform electric field, Phys. Rev. B **99**, 064426 (2019).

[26] E. Raimondo, E. Saugar, J. Barker, D. Rodrigues, A. Giordano, M. Carpentieri, W. Jiang, O. Chubykalo-Fesenko, R. Tomasello, and G. Finocchio, Temperature-Gradient-Driven Magnetic Skyrmion Motion, Phys. Rev. Appl. **18**, 024062 (2022).

[27] R. Tomasello, S. Komineas, G. Siracusano, M. Carpentieri, and G. Finocchio, Chiral skyrmions in an anisotropy gradient, Phys. Rev. B **98**, 024421 (2018).

[28] L.-M. Kern, B. Pfau, V. Deinhart, M. Schneider, C. Klose, K. Gerlinger, S. Wittrock, D. Engel, I. Will, C. M. Günther, *et al.*, Deterministic generation and guided motion of magnetic skyrmions by focused He+-ion irradiation, Nano Lett. **10**, 4028 (2022).

[29] M. Weißenhofer and U. Nowak, Topology dependence of skyrmion Seebeck and skyrmion Nernst effect, Sci. Rep. **12**, 6801 (2022).

[30] L. Chotorlishvili, X.-G. Wang, Z. Toklikishvili, and J. Berakdar, Thermoelastic enhancement of the magnonic spin Seebeck effect in thin films and bulk samples, Phys. Rev. B **97**, 144409 (2018).

[31] X.-G. Wang, L. Chotorlishvili, and J. Berakdar, Strain and thermally induced magnetic dynamics and spin current in magnetic insulators subject to transient optical grating, Front. Mater. **4**, 19 (2017).

[32] G. Ju, Y. Peng, E. K. C. Chang, Y. Ding, A. Q. Wu, X. Zhu, Y. Kubota, T. J. Klemmer, H. Amini, L. Gao, *et al.*, High density heat-assisted magnetic recording media and advanced characterization—progress and challenges, IEEE Trans. Magn. **51**, 3201709 (2015).

[33] S. Crain, E. Mount, S. Baek, and J. Kim, Individual addressing of trapped 171Yb+ ion qubits using a microelectromechanical systems-based beam steering system, Appl. Phys. Lett. **105**, 181115 (2014).

[34] A. Tuantranont, V. M. Bright, J. Zhang, W. Zhang, J. A. Neff, and Y. C. Lee, Optical beam steering using MEMS-controllable microlens array, Sens. Actuators, A **91**, 363 (2001).

[35] J. Zhang, T. Nguyen, B. Potsaid, V.r Jayaraman, C. Burgner, S. Chen, J. Li, K. Liang, A. Cable, G. Traverso, H. Mashimo, and J. G. Fujimoto, Multi-MHz MEMS-VCSEL swept-source optical coherence tomography for endoscopic structural and angiographic imaging with miniaturized brushless motor probes, Biomed. Opt. Express **12**, 2384 (2021).

[36] T. L. Gilbert, A phenomenological theory of damping in ferromagnetic materials, IEEE Trans. Magn. **40**, 3443 (2004).

[37] A. J. Newell, W. Williams, and D. J. Dunlop, A generalization of the demagnetizing tensor for nonuniform magnetization, J. Geophys. Res. Solid Earth **98**, 9551 (1993).

[38] D. A. Garanin, Fokker-Planck and Landau-Lifshitz-Bloch equations for classical ferromagnets, Phys. Rev. B **55**, 3050 (1997).

[39] H. B. Callen and E. Callen, The present status of the temperature dependence of magnetocrystalline anisotropy, and the power law, J. Phys. Chem. Sol. **27**, 1271 (1966).

[40] U. Atxitia, D. Hinzke, O. Chubykalo-Fesenko, U. Nowak, H. Kachkachi, O. N. Mryasov, R. F. Evans, and R. W. Chantrell, Multiscale modeling of magnetic materials: Temperature dependence of the exchange stiffness, Phys. Rev. B **82**, 134440 (2010).

[41] L. Rozsa, U. Atxitia, and U. Novak, Temperature scaling of the Dzyaloshinsky-Moriya interaction in the spin wave spectrum, Phys. Rev. B **96**, 094436 (2017).

[42] J. Virieux, P-SV wave propagation in heterogeneous media: Velocity-stress finite-difference method, Geophysics **51**, 889 (1986).

[43] H. N. Pishkenari, F. Samie Yousefi, and A. Taghibakhshi, Determination of surface properties and elastic constants of FCC metals: a comparison among different EAM potentials in thin film and bulk scale, Mater. Res. Express **6**, 015202 (2018).

[44] S. Yang, L. Zhang, and Y. Wei, Model-based image quality optimization for submicron direct laser writing, AIP Adv. **10**, 125121 (2020).

[45] S. Lepadatu, Interaction of magnetization and heat dynamics for pulsed domain wall movement with Joule heating, J. Appl. Phys. **120**, 163908 (2016).

[46] N. Figueiredo-Prestes, J. Zarpellon, D. da Silva Costa, I. Mazzaro, P. César de Camargo, A. J. A. de Oliveira, C. Deranlot, J.-M. George, and D. H. Mosca, Thermal stability of ultrathin Co/Pt multilayers, J. Phys. Chem. C **125**, 4885 (2021).

[47] A. A. Thiele, Steady-State Motion of Magnetic Domains, Phys. Rev. Lett. **30**, 230 (1973).

[48] S. J. Yuan, L. Sun, H. Sang, J. Du, and S. M. Zhou, Interfacial effects on magnetic relaxation in Co/Pt multilayers, Phys. Rev. B **68**, 134443 (2003).

[49] Supplemental Material at http://link.aps.org/supplemental/10.1103/PhysRevApplied.19.044036 for details on effect of magnetoelastic coupling sign, absorbed power dependences of temperature change, energy densities, and skyrmion diameter, skyrmion deformation at higher powers, further details on skyrmion lattices, and skyrmion tracking algorithm.

[50] L. Shen, J. Xia, G. Zhao, X. Zhang, M. Ezawa, O. A. Tretiakov, X. Liu, and Y. Zhou, Dynamics of the antiferromagnetic skyrmion induced by a magnetic anisotropy gradient, Phys. Rev. B **98**, 134448 (2018).

[51] H. Du, R. Che, L. Kong, X. Zhao, C. Jin, C. Wang, J. Yang, W. Ning, R. Li, C. Jin, *et al.*, Edge-mediated skyrmion chain and its collective dynamics in a confined geometry, Nat. Commun. **6**, 8504 (2015).

[52] X. Zhang, G. P. Zhao, H. Fangohr, J. P. Liu, W. X. Xia, J. Xia, and F. J. Morvan, Skyrmion-skyrmion and skyrmion-edge repulsions in skyrmion-based racetrack memory, Sci. Rep. **5**, 7643 (2015).

[53] Z. Tian, D. Sander, and J. Kirschner, Nonlinear magnetoelastic coupling of epitaxial layers of Fe, Co, and Ni on Ir(100), Phys. Rev. B **79**, 024432 (2009).

[54] E. A. Karhu, U. K. Roßler, A. N. Bogdanov, S. Kahwaji, B. J. Kirby, H. Fritzsche, M. D. Robertson, C. F. Majkrzak, and T. L. Monchesky, Chiral modulations and reorientation effects in MnSi thin films, Phys. Rev. B **85**, 094429 (2012).

[55] Y. Nii, T. Nakajima, A. Kikkawa, Y. Yamasaki, K. Ohishi, J. Suzuki, Y. Taguchi, T. Arima, Y. Tokura, and Y. Iwasa, Uniaxial stress control of skyrmion phase, Nat. Commun. **6**, 8539 (2015).

[56] Y. Nii, A. Kikkawa, Y. Taguchi, Y. Tokura, and Y. Iwasa, Elastic Stiffness of a Skyrmion Crystal, Phys. Rev. Lett. **113**, 267203 (2014).

[57] R. Zuberek, K. Fronc, W. Paszkowicz, and H. Szymczak, Magnetic anisotropy and magnetoelastic constants of ultrathin Fe/GaAs(001) films sputtered in hydrogen atmosphere, J. Magn. Magn. Mater. **283**, 28 (2004).

[58] G. A. Marchant, C. E. Patrick, and J. B. Staunton, Ab initio calculations of temperature-dependent magnetostriction of Fe and A2 $Fe_{1-x}Ga_x$ within the disordered local moment picture, Phys. Rev. B **99**, 054415 (2019).

[59] A. Enders, D. Sander, and J. Kirschner, Strain dependence of the magnetic properties of nm Fe films on W(1000), J. Appl. Phys. **85**, 5279 (1999).

[60] G. Bochi, C. A. Ballentine, H. E. Inglefield, C. V. Thompson, R. C. O'Handley, H. J. Hug, B. Stiefel, A. Moser, and H.-J. Guntherodt, Perpendicular magnetic anisotropy, domains, and misfit strain in epitaxial $Ni/Cu_{1-x}Ni_x/Cu/Si(001)$ thin films, Phys. Rev. B **52**, 7311 (1995).

[61] T. Gutjahr-Löser, D. Sander, and J. Kirschner, Magnetoelastic coupling in Co thin on W(0 0 1), J. Magn. Magn. Mater. **220**, L1 (2000).

[62] R. Juge, S. Je, D. Chaves, L. D. Buda-Prejbeanu, J. Peña-Garcia, J. Nath, I. M. Miron, K. G. Rana, L. Aballe, M. Foerster, *et al.*, Current-Driven Skyrmion Dynamics and Drive Dependent Skyrmion Hall Effect in an Ultrathin Film, Phys. Rev. Appl. **12**, 044007 (2019).

[63] K. Litzius, J. Leliaert, P. Bassirian, D. Rodrigues, S. Kromin, I. Lemesh, J. Zazvorka, K. Lee, J. Mulkers, N. Kerber, *et al.*, The role of temperature and drive current in skyrmion dynamics, Nat. Electron. **3**, 30 (2020).

[64] C. R. MacKinnon, K. Zeissler, S. Finizio, J. Raabe, C. H. Marrows, T. Mercer, P. R. Bissell, and S. Lepadatu, Collective skyrmion motion under the influence of an additional interfacial spin-transfer torque, Sci. Rep. **12**, 10786 (2022).

[65] X. Liang, G. Zhao, L. Shen, J. Xia, L. Zhao, X. Zhang, and Y. Zhou, Dynamics of an antiferromagnetic skyrmion in a racetrack with a defect, Phys. Rev. B **100**, 144439 (2019).

[66] S. Lepadatu, Effective field model of roughness in magnetic nano-structures, J. Appl. Phys. **118**, 243908 (2015).

[67] C. Gong, Y. Zhou, and G. Zhao, Dynamics of magnetic skyrmions under temperature gradients, Appl. Phys. Lett. **120**, 052402 (2022).

[68] L. Shen, J. Xia, G. Zhao, X. Zhang, M. Ezawa, O. A. Tretiakov, X. Liu, and Y. Zhou, Spin torque nano-oscillators based on antiferromagnetic skyrmions, Appl. Phys. Lett. **114**, 042402 (2019).

[69] X. Liang, X. Zhang, J. Xia, M. Ezawa, Y. Zhao, G. Zhao, and Y. Zhou, A spiking neuron constructed by the skyrmion-based spin torque nano-oscillator, Appl. Phys. Lett. **116**, 122402 (2020).

[70] T. Dohi, S. Dutta Gupta, S. Fukami, and H. Ohno, Formation and current-induced motion of synthetic antiferromagnetic skyrmion bubbles, Nat. Commun. **10**, 5153 (2019).

[71] S. Lepadatu, Boris computational spintronics — high performance multi-mesh magnetic and spin transport modeling software, J. Appl. Phys. **128**, 243902 (2020).

[72] J. W. Thomas, *Numerical Partial Differential Equations: Finite Difference Methods* (Springer-Verlag, New York, 1995).

[73] S. Lepadatu, Speeding up explicit numerical evaluation methods for micromagnetic simulations using demagnetizing field polynomial extrapolation, IEEE Trans. Magn. **58**, 1300706 (2022).